Showcasing research from Professor Guanjun Xiao's research group, State Key Laboratory of Superhard Materials, College of Physics, Jilin University, Changchun 130012, China.

Self-trapped exciton emission and piezochromism in conventional 3D lead bromide perovskite nanocrystals under high pressure

We successfully achieved self-trapped exciton emission with outstanding white light chromaticity coordinates of (0.330, 0.325) in the conventional 3D halide perovskite nanocrystals through pressure engineering.

As featured in:

See Guanjun Xiao *et al.*,
Chem. Sci., 2021, **12**, 14711.

ROYAL SOCIETY
OF **CHEMISTRY**

rsc.li/chemical-science

Check for updates

Self-trapped exciton emission and piezochromism in conventional 3D lead bromide perovskite nanocrystals under high pressure†

Yue Shi, Wenya Zhao, Zhiwei Ma, Guanjun Xiao 🄳 * and Bo Zou 🄳

Developing single-component materials with bright-white emission is required for energy-saving applications. Self-trapped exciton (STE) emission is regarded as a robust way to generate intrinsic white light in halide perovskites. However, STE emission usually occurs in low-dimensional perovskites whereby a lower level of structural connectivity reduces the conductivity. Enabling conventional three-dimensional (3D) perovskites to produce STEs to elicit competitive white emission is challenging. Here, we first achieved STEs-related emission of white light with outstanding chromaticity coordinates of (0.330, 0.325) in typical 3D perovskites, Mn-doped $CsPbBr_3$ nanocrystals (NCs), through pressure processing. Remarkable piezochromism from red to blue was also realized in compressed Mn-doped $CsPbBr_3$ NCs. Doping engineering by size-mismatched Mn dopants could give rise to the formation of localized carriers. Hence, high pressure could further induce octahedra distortion to accommodate the STEs, which has never occurred in pure 3D perovskites. Our study not only offers deep insights into the photophysical nature of perovskites, it also provides a promising strategy towards high-quality, stable white-light emission.

Introduction

Lighting equipment is an important part of daily life. Recently, single-component materials with white emission typically originating from self-trapped excitons (STEs) have become appealing options for solid-state lighting applications. This is because they have a simplified device structure, and avoid the self-absorption and color instability seen in traditional multiple emitters.[1] The radiative recombination of STEs in low-dimensional metal halide perovskites (LMHPs) has been investigated widely, but the lower level of structural connectivity of metal halide octahedra in LMHPs reduces conductivity, which seriously limits their practical application in optoelectric devices.[2,3] The three-dimensional (3D) perovskites $CsPbX_3$ (X = Cl, Br, I) have excellent charge-transport properties. They are regarded as deal candidates for high-efficiency light-emitting diodes because of high quantum efficiency, high color purity, and easy tunability of wavelengths.[4–8] However, realization of white emission based on STEs in 3D perovskite materials is challenging.

High-pressure studies on metal halide perovskite (MHP) materials have revealed increases in optical tuning,[2,9–11]

bandgap optimization,[12,13] morphological control[6,14–17] and dramatic increases in quantum yields.[18–21] In particular, a new concept of pressure induced emission (PIE), whereby a non-luminescent material exhibits emission upon compression, was proposed in the research of compressed zero-dimensional (0D) perovskite Cs_4PbBr_6 nanocrystals (NCs).[22] Thus, PIE provides distinct advantages for light-emitting applications achievable by the design of structural distortion.[23–26] Localization of carriers resulting from a low electronic dimension and seriously distorted metal halide octahedra enhance the optical activity and binding energy of STEs. Therefore, the radiative recombination of STEs may also be activated in doped 3D perovskite materials with local carriers by continuously tuning the structural distortion with the assistance of a high-pressure method.

The dopant Mn^{2+} has been studied extensively in $CsPbBr_3$ NCs. Its excited carriers within the host perovskite excitation are trapped into Mn^{2+}, leading to the formation of local electrons *via* energy transfer.[27–30] Doping Mn^{2+} in $CsPbBr_3$ induces the local distortion of the octahedral framework considerably, in contrast to the case of $CsPbCl_3$ NCs.[31] This phenomenon occurs because of the greater disparity of M–Br (M = Pb, Mn) bond-dissociation energies between $PbBr_2$ (249 kJ mol^{-1}) and $MnBr_2$ (314 kJ mol^{-1}) compared with $PbCl_2$ (301 kJ mol^{-1}) and $MnCl_2$ (338 kJ mol^{-1}) precursors.[32] Motivated by such results, we were encouraged to systematically investigate the pressure response of replacing Mn^{2+} with Pb^{2+} within $CsPbBr_3$ NCs. We documented significant enhancement of broadband emission

State Key Laboratory of Superhard Materials, College of Physics, Jilin University, Changchun 130012, China. E-mail: xguanjun@jlu.edu.cn

in doped 3D all-inorganic halide perovskites, $CsPb_xMn_{1-x}Br_3$ NCs, under 7.62 GPa, where the emissive color transferred to expected white light from the initial orange. An isostructural phase transformation at ~2.00 GPa was demonstrated by *in situ* high-pressure angle dispersive synchrotron X-ray diffraction (ADXRD) and optical absorption. The large uneven lattice deformation around the Mn dopants accommodates the STEs, and exciton self-trapping never occurs in pure $CsPbBr_3$. We not only discovered an effective approach to enhance the broadband emission originating from STEs in doped 3D all-inorganic perovskites $CsPb_xMn_{1-x}Br_3$ NCs, we also provide insights into the microscopic mechanisms that could guide future designs for materials with light-emitting applications.

Results and discussion

The morphology and structure of the synthesized Mn-doped $CsPbBr_3$ NCs were investigated using transmission electron microscopy (TEM) and high-resolution TEM (HRTEM) characterizations. As shown in Fig. S1a–c,† the samples before compression exhibited a nanocube morphology with good crystallinity. The Mn-doped $CsPbBr_3$ NCs had an average diameter of 9.28 nm with a standard deviation of 1.07 nm. Under an ambient condition, the photoluminescence (PL) spectrum (Fig. 1a) revealed dual emission peaks centered at ~439 nm ($CsPb_xMn_{1-x}Br_3$ band-edge emission) and 613 nm (Mn-related emission), which are consistent with previous reports.[32] *In situ* high-pressure PL measurement of

$CsPb_xMn_{1-x}Br_3$ NCs was carried out to investigate optical properties up to 19 GPa (Fig. 1a–c and S2†). With an increase in pressure, the intensity of the band-edge PL peak experienced weakening and vanished completely at 2.05 GPa, whereas the Mn-related emission declined slightly before 0.90 GPa. Upon further compression to 2.05 GPa, the intensity of Mn-related emission strengthened sharply. Both peaks showed a red shift below 2.05 GPa. When the applied pressure exceeded 2.05 GPa, a new emission appeared and experienced persistent enhancement in its intensity with increasing pressure. This new emission could be clearly fitted by two sub-bands denoted as Peak I and Peak II in Fig. S3,† which are located around ~448 and ~508 nm, respectively. Peak I and Peak II first exhibited a red shift with increasing pressure until 5.16 GPa, then the peak position of two emissions was virtually unchanged. Detailed information about the new emission is shown in Table S1 and Fig. S4.† Interestingly, the new emission exhibited excellent stability, and suppressed the general emission quenching at high pressure. Even up to 19 GPa, the new emission had reasonable emissive properties. Furthermore, the CIE chromaticity coordinates of Mn-doped $CsPbBr_3$ NCs could be controlled effectively by pressure across a wide range from red to blue, which was corroborated clearly from the change of emission color throughout compression (Fig. 1d, e and Table 1). High-quality white-light emission with chromaticity coordinates of (0.330, 0.325) were obtained through pressure processing. The ability to achieve white emission in 3D perovskites with tunable chromaticity indicated a prospective strategy for creating
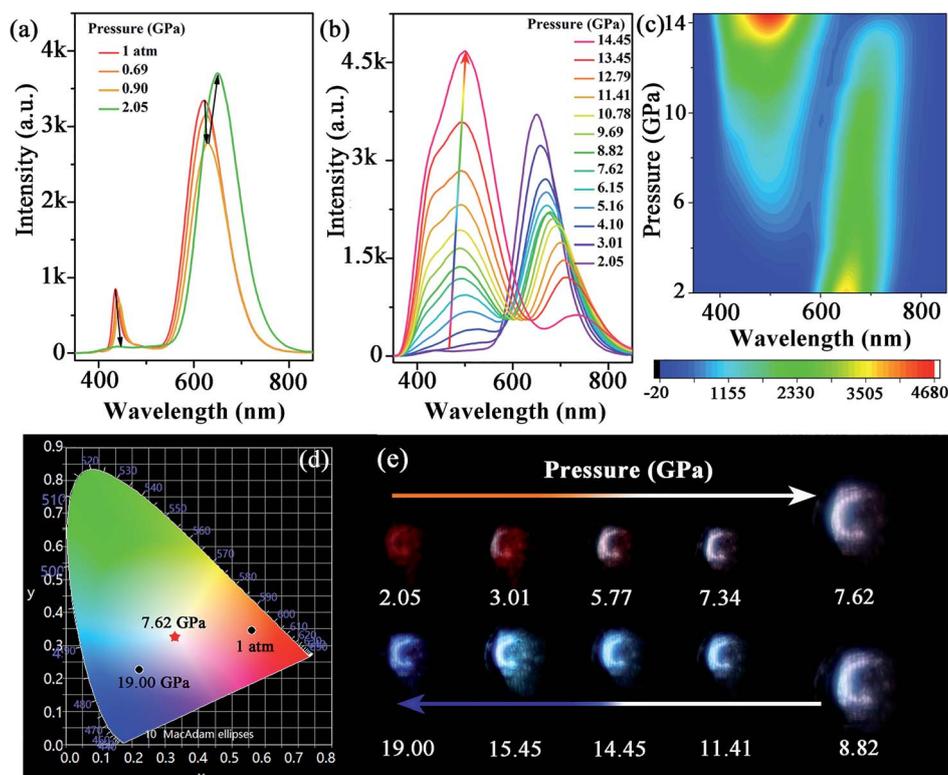

Fig. 1 (a–c) PL spectra of Mn-doped $CsPbBr_3$ NCs under high pressure. (d) Pressure-dependent chromaticity coordinates of the emissions. (e) PL micrographs upon compression.

Table 1 Chromaticity coordinates at selected pressures for $CsPb_x$-$Mn_{1-x}Br_3$ NCs

Pressure (GPa)	CIE x	CIE y	Pressure (GPa)	CIE x	CIE y
1 atm	0.561	0.345	10.78	0.260	0.309
2.05	0.626	0.338	11.41	0.241	0.302
4.10	0.504	0.358	13.45	0.229	0.309
5.16	0.432	0.356	14.45	0.232	0.328
6.64	0.366	0.338	17.00	0.234	0.275
7.62	0.330	0.325	18.00	0.229	0.252
8.82	0.307	0.317	19.00	0.222	0.226
9.69	0.276	0.310			

colorful solar designs using strain/pressure engineering with reasonable chemical regulation or device construction. When the pressure was released completely, the PL spectra of pressure-treated samples showed a distinct difference compared with that in its initial state (Fig. S5†), which exhibited Mn^{2+}-dominated emission. To provide insights into this phenomenon, we further investigated the morphology and structure of Mn-doped $CsPbBr_3$ NCs after decompression using TEM and HRTEM characterizations. The quenched samples exhibited deformation to some extent, with relatively poor crystallinity (Fig. S6†), which led to an increase in defects. Therefore, the defects produced after pressure processing would result in suppression of band-edge emission.

We also undertook *in situ* high-pressure ultraviolet-visible (UV-Vis) absorption measurements up to ~23.98 GPa (Fig. 2a). At the ambient condition, the absorption edge of $CsPb_x$-$Mn_{1-x}Br_3$ NCs was ~440 nm, a blue shift compared with perfect $CsPbBr_3$ NCs.[33] Upon compression, the absorption spectra
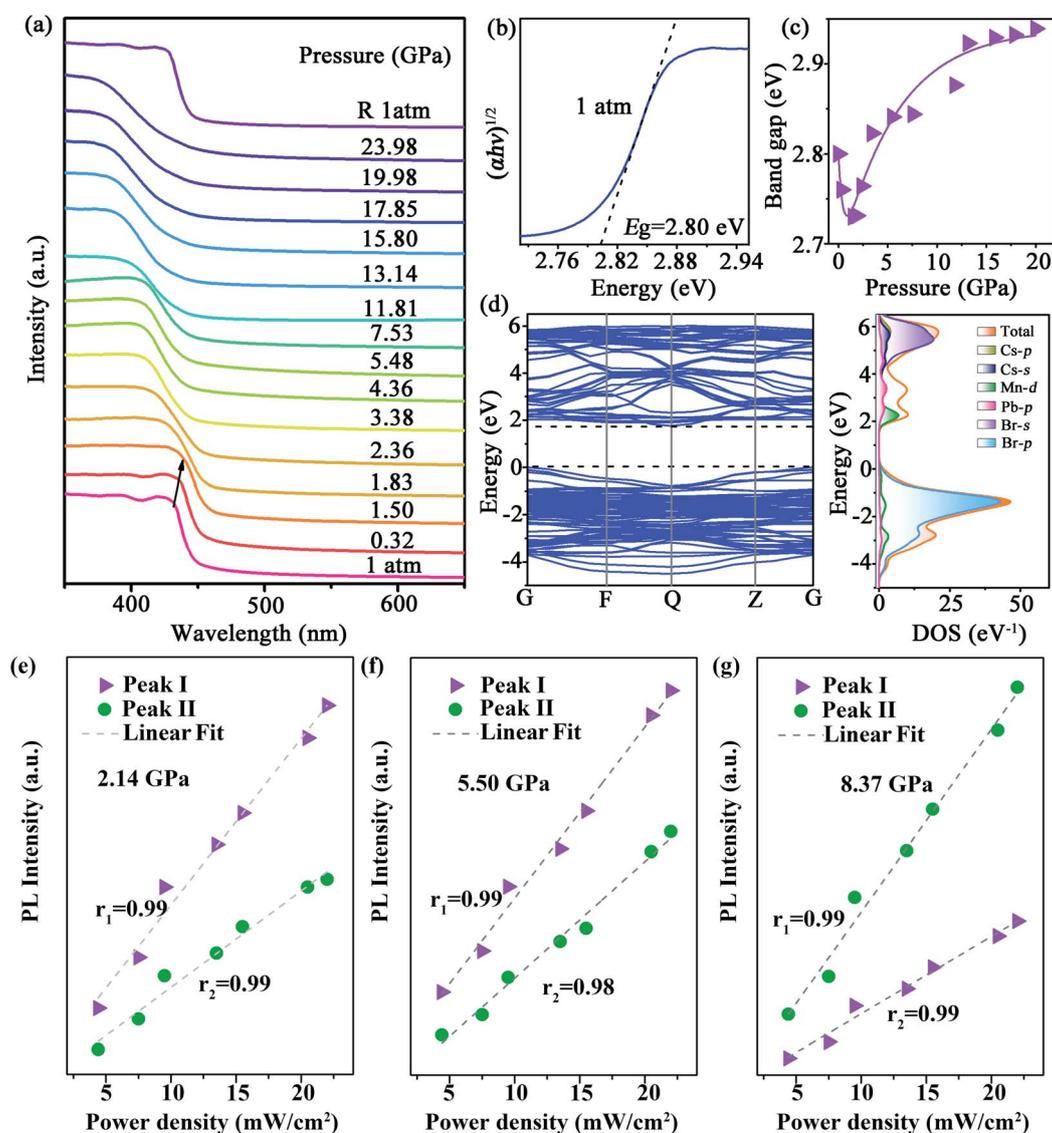

Fig. 2 (a) Absorption spectra of $CsPb_xMn_{1-x}Br_3$ NCs as a function of pressure. (b) Indirect bandgap Tauc plot for $CsPb_xMn_{1-x}Br_3$ NCs at ambient pressure. (c) Bandgap evolution of $CsPb_xMn_{1-x}Br_3$ NCs as a function of pressure. (d) Left: calculated electron-band structure of $CsPb_xMn_{1-x}Br_3$ NCs at 1 atm. Right: total and partial density of states projected on the orbitals of different atoms. PL intensity of emission Peak I and Peak II at 2.14 GPa (e), 5.50 GPa (f) and 8.37 GPa (g) as a function of power density. The intensity of Peak I is denoted as triangular purple dots, whereas the intensity of Peak II is denoted as circular green dots.

showed a red shift before 1.83 GPa. After that, the bandgap increased suddenly, which was coincident with emergence of a new PL peak. The indirect bandgap of $CsPb_xMn_{1-x}Br_3$ NCs was estimated by extrapolating the linear portion of $(\alpha h\upsilon)^{1/2}$ versus $h\upsilon$ in Tauc plots, where α is the absorption coefficient and $h\upsilon$ is the photon energy. The bandgap value (E_g) of $CsPb_x\text{-}Mn_{1-x}Br_3$ NCs was ~2.80 eV at the ambient condition (Fig. 2b). At a relatively low pressure of 1.50 GPa, E_g exhibited linear narrowing by 0.07 eV (Fig. 2c) that was related to lattice contraction.[33] Upon further compression, the rate of photon energy increased sharply above 1.83 GPa (Fig. 2c and S7†). This sudden change in bandgap energy could be attributed to distortion of inorganic octahedra.[34] Density functional theory (DFT) calculations revealed that the indirect bandgap of $CsPb_xMn_{1-x}Br_3$ NCs was determined mainly by changes in the valence band maximum (VBM) and conduction band minimum (CBM) (Fig. 2d). The distinctly different evolution between emission Peak I, Peak II and absorption edge associated with free excitons ruled out a mechanism based on band-edge transition.[35] Furthermore, the new emissions showed a gradual red shift, whereas the band edge showed a gradual blue shift, resulting in a large increase in the Stokes shift

(Fig. S4a†), which could be ascribed to the enhanced strength of electron–phonon coupling. Likewise, the intensity of Peak I and Peak II at different pressures showed a linear dependence on the excitation power density up to 22 mW cm^{-2} (Fig. 2e–g), indicating that both emissions originated from STEs.[36,37] Typically, the presence of STEs was manifested through broadband luminescence.[38] Once electrons and holes are photogenerated, they are self-trapped rapidly to form STEs due to the strong electron–phonon coupling with an increase in pressure, which leads to the emission enhancement of STEs.[22,39]

To verify the correlation between the optical properties and structural distortion of $CsPb_xMn_{1-x}Br_3$ NCs, *in situ* high-pressure ADXRD experiments were undertaken. At the ambient condition, all diffraction peaks exhibited slight broadening, which could have been related to the uneven distortion among $PbBr_6$ and $MnBr_6$ octahedra. Upon compression, all diffraction peaks shifted to higher 2θ angles due to lattice contraction (Fig. 3a). Although the changes in PL and absorption spectra were obvious at 2.05 GPa, the ADXRD patterns over different pressures barely changed. This observation suggested isostructural phase transition in $CsPb_xMn_{1-x}Br_3$ NCs, which are (in general) considered to be derived from electronic structural transitions (see ESI†). The

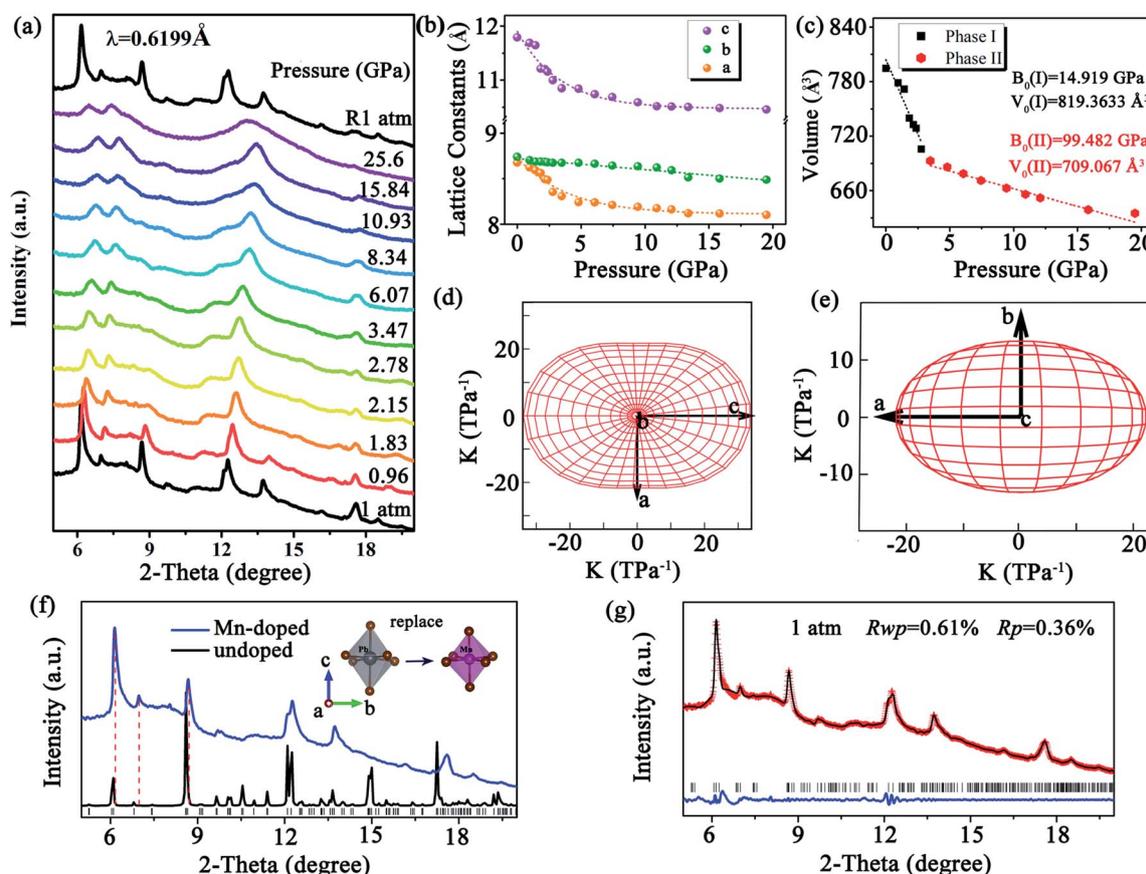**Fig. 3** (a) Representative *in situ* high-pressure ADXRD patterns of $CsPb_xMn_{1-x}Br_3$ NCs. (b) Pressure-dependent lattice constants of $CsPb_x\text{-}Mn_{1-x}Br_3$ NCs. (c) Cell-volume evolution of $CsPb_xMn_{1-x}Br_3$ NCs upon compression. (d and e) Polar compressibility indicatrix in the *ab* and *ac* planes of $CsPb_xMn_{1-x}Br_3$ NCs. (f) ADXRD pattern of $CsPb_xMn_{1-x}Br_3$ NCs, along with the reference ADXRD pattern for the orthorhombic phase of $CsPb_xMn_{1-x}Br_3$. Inset shows the partial cation exchange in $CsPbBr_3$ NCs (schematic). Therein, Pb^{2+} are partially replaced by Mn^{2+}, thereby resulting in divalent-cation-doped $CsPb_{1-x}Mn_xBr_3$ NCs. (g) Refinements of experimental (red fork), simulated (black profile), and different (blue line) ADXRD patterns at 1 atm. Therein, black vertical markers indicate the corresponding Bragg reflections.

pressure-induced rotation of PbBr$_6$ and MnBr$_6$ octahedra with an opposite direction and structural distortion were responsible for the isostructural phase transition. At higher pressures, CsPb$_x$Mn$_{1-x}$Br$_3$ NCs tended to be amorphous, and only a few broad diffraction peaks were detected. Comparison of the peak positions to those of pure CsPbBr$_3$ revealed the ADXRD peaks of CsPb$_x$Mn$_{1-x}$Br$_3$ NCs to shift towards higher diffraction angles. This phenomenon indicated lattice contraction owing to the substitution of Pb^{2+} by smaller Mn^{2+} in host lattices (Fig. 3f). Refined ADXRD data at 1 atm agreed well with experimental data ($R_{wp} = 0.61\%$ and $R_P = 0.36\%$) (Fig. 3g). The lattice constants for different axes of CsPb$_x$Mn$_{1-x}$Br$_3$ NCs were collected as a function of pressure (Fig. 3b). The compressed rate of a and c axes experienced a turning point at >2.15 GPa, which matched closely with changes in PL and absorption. The discontinued evolution of lattice parameters at 2.15 GPa were ascribed to the isostructural phase transition. The bulk modulus (B_0) of CsPb$_x$Mn$_{1-x}$Br$_3$-NCs was obtained by fitting the pressure-dependent unit-cell volumes based on the Birch–Murnaghan equation of state. Note that the B_0 after isostructural phase transition was much larger

than the initial value (14.91 GPa), indicating the less compressible nature of high-pressure structure (Fig. 3c). Moreover, the polar compressibility indicatrix in the ac and ab planes revealed obvious anisotropy within the structure (Fig. 3d and e).

We revealed the distortion of Mn–Br and Pb–Br octahedra within CsPb$_x$Mn$_{1-x}$Br$_3$ under pressure quantitatively (Fig. 4a and b). The degree of octahedral distortions was determined using the following parameters:[11]

Distortion of bond length:

$$\Delta d = \frac{1}{6} \sum_{i=1}^{6} [(d_i - d_0)/d_0]^2 \tag{1}$$

Variance in octahedral angle:

$$\delta^2 = \frac{1}{11} \sum_{i=1}^{12} (\theta_i - 90)^2 \tag{2}$$

where d_0 is the average bond length of Pb–Br or Mn–Br, d_i represents the individual bond lengths of Pb–Br or Mn–Br, and θ_i represents the individual Br–Pb/Mn–Br bond angles of the
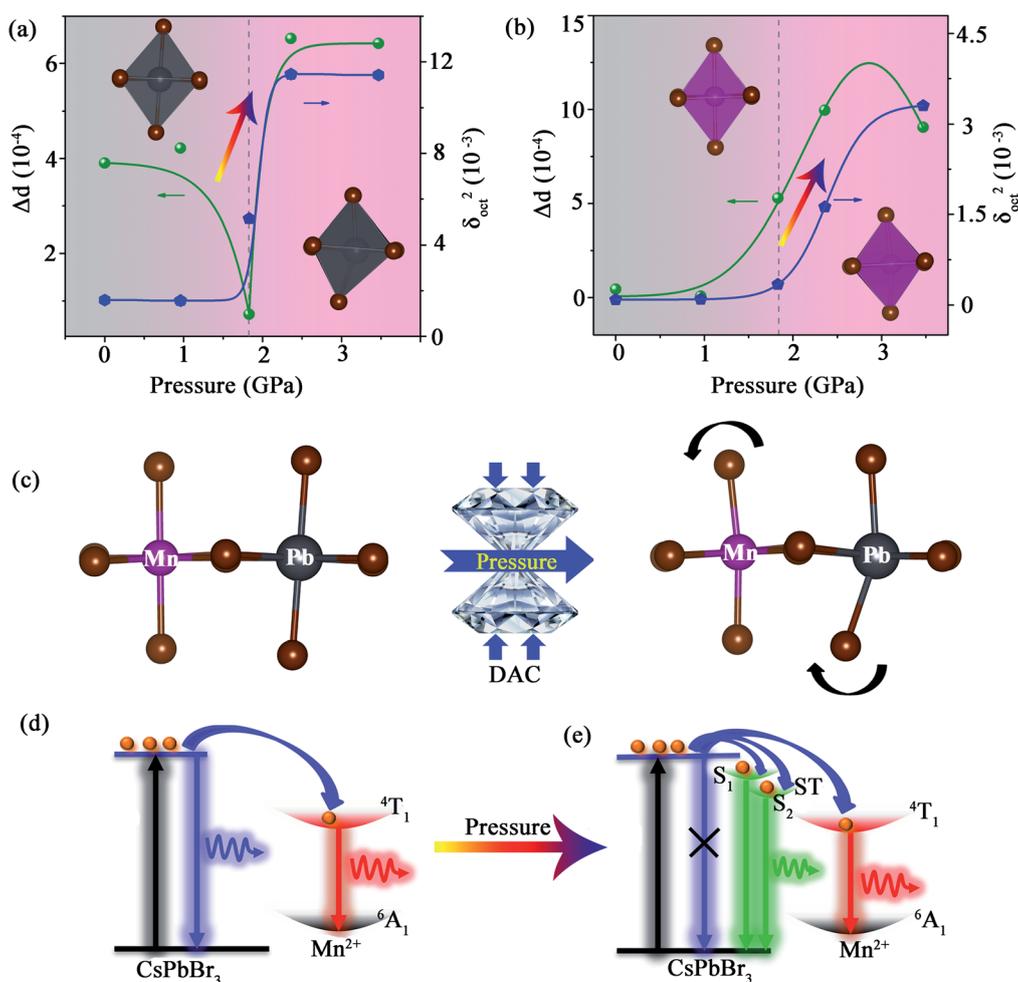

Fig. 4 (a) δ^2 values (variance in octahedral angle) and Δd values (distortion in bond length) of Pb octahedra within CsPb$_x$Mn$_{1-x}$Br$_3$ NCs under pressure. (b) δ^2 values and Δd values of Mn octahedra within CsPb$_x$Mn$_{1-x}$Br$_3$ NCs under pressure. (c) Crystal structures viewed along the a axis of CsPb$_x$Mn$_{1-x}$Br$_3$ NCs before and after compression. Configuration coordinate models for CsPb$_x$Mn$_{1-x}$Br$_3$ NCs at ambient pressure (d) and high pressure (e). ST denotes self-trapped states.

octahedron. Distinctively different degrees of distortion between $PbBr_6$ and $MnBr_6$ octahedra within the initial structure were attributed to the disparity in bond-dissociation energies between Mn–Br and Pb–Br (bond dissociation energy for $PbBr_2 = 249$ kJ mol^{-1} and for $MnBr_2 = 314$ kJ mol^{-1}). Therefore, the localized carriers formed readily around the more distorted $MnBr_6$ octahedra. As the pressure approached 2.15 GPa, the rotation of octahedra became severe (Fig. 4c), which triggered more distortion and led to stronger electron–phonon coupling. This phenomenon would result in enhancement of the activation energy for detrapping, and more STEs would be stabilized to give rise to intriguing PIE. The mechanism for white-light emission for $CsPb_xMn_{1-x}Br_3$ NCs upon compression is shown in Fig. 4d and e. The band-edge emission of $CsPb_xMn_{1-x}Br_3$ NCs was caused by the energy release (blue arrow) from the excitonic state to the ground state, which we considered to be channel 1. Meanwhile, the energy transfer from the excitonic state to $^4T_1$ state of Mn^{2+} occurred, after which the inherent transition from $^4T_1$ to $^6A_1$ of the Mn ion (channel 2) induced a new emission at 613 nm (red arrow).[28,40–42] In addition, octahedra with different degrees of distortion, owing to the substitution of Pb^{2+} by smaller Mn^{2+} in host lattices, resulted in localized carriers. When the pressure reached 2.15 GPa, $CsPb_xMn_{1-x}Br_3$ NCs experienced an isostructural phase transition. The radiation energy from the excitonic state to the ground state (blue arrow) of $CsPb_xMn_{1-x}Br_3$ NCs was suppressed, thereby leading to enhancement in the energy transfer branching ratio from the excitonic state to Mn state, accompanied by intensity quenching of the PL peak at 406 nm. Furthermore, the large uneven lattice deformation around the Mn impurities accommodated the STEs, where exciton self-trapping never occurs in its pure perovskite state.[38] With the large increase in electron–phonon coupling and detrapping barrier, the broadband PIE of STEs was reasonably allowed at high pressure (green arrow in Fig. 4e). Accordingly, the exotic white-light emission in Mn^{2+}-doped conventional 3D halide perovskite $CsPbBr_3$ NCs was achieved as expected.

Conclusions

We realized, for the first time, high-quality white-light emission with chromaticity coordinates of (0.330, 0.325) by designing STEs formation in dense traditional 3D perovskite Mn-doped $CsPbBr_3$ NCs. The size-mismatched 3D-perovskite structure resulting from the introduction of Mn dopants and the subsequent large distortion suppressed radiative recombination of free excitons and stabilized more STEs resulting, ultimately, in STE emission. Moreover, considerable piezochromism and intriguing PIE associated with STEs were discovered under high pressure. Our study not only deepens insight into PIE, but also provides guidelines to improve the designability of stable white-emission 3D perovskites for solid-state lighting and displays.

Data availability

Data are available within the article or its ESI materials.† The data that cannot be found in the article or in ESI materials† are available on request from the authors.

Author contributions

J. X. and B. Z. devised the method and conceived the project. Y. S. designed and performed the experiments. W. Z. and Z. M. performed the partial experiments and calculations. All authors analyzed the results and contributed to writing the manuscript. All authors have given approval to the final version of the manuscript.

Conflicts of interest

There are no conflicts to declare.

Acknowledgements

Notes and references

1 S. Pathak, N. Sakai, F. Wisnivesky Rocca Rivarola, S. D. Stranks, J. Liu, G. E. Eperon, C. Ducati, K. Wojciechowski, J. T. Griffiths, A. A. Haghighirad, A. Pellaroque, R. H. Friend and H. J. Snaith, *Chem. Mater.*, 2015, **27**, 8066–8075.

2 S. Sun, C. K. Gan, A. G. del Águila, Y. Fang, J. Xing, T. T. H. Do, T. J. White, H. Li, W. Huang and Q. Xiong, *Sci. Adv.*, 2019, **5**, eaav9445.

3 Z. Yang, C. Qin, Z. Ning, M. Yuan, J. Tang and L. Ding, *Sci. Bull.*, 2020, **65**, 1057–1060.

4 L. Protesescu, S. Yakunin, M. I. Bodnarchuk, F. Krieg, R. Caputo, C. H. Hendon, R. X. Yang, A. Walsh and M. V. Kovalenko, *Nano Lett.*, 2015, **15**, 3692–3696.

5 J. Song, J. Li, X. Li, L. Xu, Y. Dong and H. Zeng, *Adv. Mater.*, 2015, **27**, 7162–7167.

6 Y. Nagaoka, K. Hills-Kimball, R. Tan, R. Li, Z. Wang and O. Chen, *Adv. Mater.*, 2017, **29**, 1606666.

7 S. Guo, K. Bu, J. Li, Q. Hu, H. Luo, Y. He, Y. Wu, D. Zhang, Y. Zhao, W. Yang, M. G. Kanatzidis and X. Lu, *J. Am. Chem. Soc.*, 2021, **143**, 2545–2551.

8 Y. Liu, B. Dong, A. Hagfeldt, J. Luo and M. Graetzel, *SmartMat*, 2021, **2**, 33–37.

9 Q. Li, Z. Chen, M. Li, B. Xu, J. Han, Z. Luo, L. Tan, Z. Xia and Z. Quan, *Angew. Chem., Int. Ed.*, 2020, **60**, 2583–2587.

10 Q. Li, Z. Chen, B. Yang, L. Tan, B. Xu, J. Han, Y. Zhao, J. Tang and Z. Quan, *J. Am. Chem. Soc.*, 2020, **142**, 1786–1791.

11 M. E. Sun, T. Geng, X. Yong, S. Lu, L. Ai, G. Xiao, J. Cai, B. Zou and S. Q. Zang, *Adv. Sci.*, 2021, **8**, 2004853.

12 Z. Ma, F. Li, D. Zhao, G. Xiao and B. Zou, *CCS Chem.*, 2020, **2**, 71–80.

13 Q. Li, Y. Wang, W. Pan, W. Yang, B. Zou, J. Tang and Z. Quan, *Angew. Chem., Int. Ed.*, 2017, **56**, 15969–15973.

14 Z. Wang and S. Saxena, *Solid State Commun.*, 2002, **123**, 195–200.

15 T. Yin, B. Liu, J. Yan, Y. Fang, M. Chen, W. K. Chong, S. Jiang, J. L. Kuo, J. Fang, P. Liang, S. H. Wei, K. P. Loh, T. C. Sum, T. J. White and Z. X. Shen, *J. Am. Chem. Soc.*, 2018, **141**, 1235–1241.

16 L. Meng, J. M. D. Lane, L. Baca, J. Tafoya, T. Ao, B. Stoltzfus, M. Knudson, D. Morgan, C. Austin, C. Park, P. Chow, Y. Xiao, R. Li, Y. Qin and H. Fan, *J. Am. Chem. Soc.*, 2020, **142**, 6505–6510.

17 T. Wang, R. Li, Z. Quan, W. S. Loc, W. A. Bassett, H. Xu, Y. C. Cao, J. Fang and Z. Wang, *Adv. Mater.*, 2015, **27**, 4544–4549.

18 Y. Wang, S. Guo, H. Luo, C. Zhou, H. Lin, X. Ma, Q. Hu, M. H. Du, B. Ma, W. Yang and X. Lu, *J. Am. Chem. Soc.*, 2020, **142**, 16001–16006.

19 Y. Wang, H. Zhang, J. Zhu, X. Lu, S. Li, R. Zou and Y. Zhao, *Adv. Mater.*, 2020, **32**, 1905007.

20 Z. Wang, C. Schliehe, T. Wang, Y. Nagaoka, Y. C. Cao, W. A. Bassett, H. Wu, H. Fan and H. Weller, *J. Am. Chem. Soc.*, 2011, **133**, 14484–14487.

21 H. Luo, S. Guo, Y. Zhang, K. Bu, H. Lin, Y. Wang, Y. Yin, D. Zhang, S. Jin, W. Zhang, W. Yang, B. Ma and X. Lu, *Adv. Sci.*, 2021, **8**, 2100786.

22 Z. Ma, Z. Liu, S. Lu, L. Wang, X. Feng, D. Yang, K. Wang, G. Xiao, L. Zhang, S. A. T. Redfern and B. Zou, *Nat. Commun.*, 2018, **9**, 4506.

23 Z. Ma, F. Li, L. Sui, Y. Shi, R. Fu, K. Yuan, G. Xiao and B. Zou, *Adv. Opt. Mater.*, 2020, **8**, 2000713.

24 X. Lü, C. Stoumpos, Q. Hu, X. Ma, D. Zhang, S. Guo, J. Hoffman, K. Bu, X. Guo, Y. Wang, C. Ji, H. Chen, H. Xu, Q. Jia, W. Yang, M. G. Kanatzidis and H.-K. Mao, *Natl. Sci. Rev.*, 2021, nwaa288.

25 S. Guo, Y. Zhao, K. Bu, Y. Fu, H. Luo, M. Chen, M. P. Hautzinger, Y. Wang, S. Jin, W. Yang and X. Lu, *Angew. Chem., Int. Ed.*, 2020, **59**, 17533–17539.

26 R. Fu, W. Zhao, L. Wang, Z. Ma, G. Xiao and B. Zou, *Angew. Chem., Int. Ed.*, 2021, **60**, 10082–10088.

27 D. Zhao, G. Xiao, Z. Liu, L. Sui, K. Yuan, Z. Ma and B. Zou, *Adv. Mater.*, 2021, **33**, 2100323.

28 D. Parobek, B. J. Roman, Y. Dong, H. Jin, E. Lee, M. Sheldon and D. H. Son, *Nano Lett.*, 2016, **16**, 7376–7380.

29 W. J. Mir, M. Jagadeeswararao, S. Das and A. Nag, *ACS Energy Lett.*, 2017, **2**, 537–543.

30 S. K. Mehetor, H. Ghosh, B. Hudait, N. S. Karan, A. Paul, S. Baitalik and N. Pradhan, *ACS Energy Lett.*, 2019, **4**, 2353–2359.

31 Y. Cao, G. Qi, L. Sui, Y. Shi, T. Geng, D. Zhao, K. Wang, K. Yuan, G. Wu, G. Xiao, S. Lu and B. Zou, *ACS Mater. Lett.*, 2020, **2**, 381–388.

32 D. Parobek, Y. Dong, T. Qiao and D. H. Son, *Chem. Mater.*, 2018, **30**, 2939–2944.

33 G. Xiao, Y. Cao, G. Qi, L. Wang, C. Liu, Z. Ma, X. Yang, Y. Sui, W. Zheng and B. Zou, *J. Am. Chem. Soc.*, 2017, **139**, 10087–10094.

34 F. Bai, K. Bian, X. Huang, Z. Wang and H. Fan, *Chem. Rev.*, 2019, **119**, 7673–7717.

35 Z. Ma, F. Li, G. Qi, L. Wang, C. Liu, K. Wang, G. Xiao and B. Zou, *Nanoscale*, 2019, **11**, 820–825.

36 J. Luo, X. Wang, S. Li, J. Liu, Y. Guo, G. Niu, L. Yao, Y. Fu, L. Gao, Q. Dong, C. Zhao, M. Leng, F. Ma, W. Liang, L. Wang, S. Jin, J. Han, L. Zhang, J. Etheridge, J. Wang, Y. Yan, E. H. Sargent and J. Tang, *Nature*, 2018, **563**, 541–545.

37 N. Pradhan, F. Liu, T. Zhang, D. Mondal, S. Teng, Y. Zhang, K. Huang, D. Wang, W. Yang, P. Mahadevan, Y. S. Zhao and R. Xie, *Angew. Chem., Int. Ed.*, 2021, **60**, 13548–13553.

38 J. Yu, J. Kong, W. Hao, X. Guo, H. He, W. R. Leow, Z. Liu, P. Cai, G. Qian, S. Li, X. Chen and X. Chen, *Adv. Mater.*, 2018, 1806385.

39 Y. Shi, Z. Ma, D. Zhao, Y. Chen, Y. Cao, K. Wang, G. Xiao and B. Zou, *J. Am. Chem. Soc.*, 2019, **141**, 6504–6508.

40 Y. Zhou, J. Chen, O. M. Bakr and H.-T. Sun, *Chem. Mater.*, 2018, **30**, 6589–6613.

41 W. Liu, Q. Lin, H. Li, K. Wu, I. Robel, J. M. Pietryga and V. I. Klimov, *J. Am. Chem. Soc.*, 2016, **138**, 14954–14961.

42 D. Rossi, D. Parobek, Y. Dong and D. H. Son, *J. Phys. Chem. C*, 2017, **121**, 17143–17149.